JTTEE5 10:666-672

Evaporation of Zirconia Powders in a Thermal Radio-Frequency Plasma

P. Buchner, H. Schubert, J. Uhlenbusch, and M. Weiss

(Submitted 16 May 2000)

Incomplete evaporation of high-melting solid precursors, such as zirconia (ZrO_2), is a major problem in the application of plasma-flash evaporation processes to powder synthesis and production of high performance coatings. The evaporation of zirconia powders injected into a thermal radio-frequency (RF) plasma is investigated by using optical emission spectroscopy (OES) and laser Doppler anemometry (LDA) to study evaporation rates and particle velocities. Model calculations are compared with the results of the process diagnostics. Axial emission profiles confirm the influence of the particle size on the evaporation behavior. Line-integrated side-on emission profiles are used to assess the rate of evaporation.

Keywords laser Doppler anemometry, nanoparticles, optical emission spectroscopy, plasma modeling, thermal RF plasma

1. Introduction

The radio-frequency (RF) generated thermal plasmas offer a 10,000 K hot region free from electrode contamination. The long residence time, compared with direct current plasma jets, for particles injected into this kind of plasma jet makes it suitable for the production of ultrafine particles and coatings. In addition to plasma spraying, where melting of injected precursor materials is sufficient, the plasma-flash evaporation technique[1] requires complete evaporation of the precursor to produce high performance coatings and nanosized powders. The method consists of an evaporation phase where the injected solid precursor materials are vaporized and partly dissociated. Rapid quenching causes a limited growth of nucleating particles or condensation of a coating on an appropriate substrate, respectively. Solids as starting materials are available at low costs for a wide class of materials, and since pure substances can be used, no unwelcome reaction products are formed. Boiling point and heat of evaporation are often much higher for the solid starting materials compared with other precursors, so special care has to be taken for the complete evaporation of the particles.

Zirconia (ZrO_2) is a material with extreme thermal properties (melting temperature: 2950 K, evaporation temperature: 4548 K[2]) that is used in technical applications, such as high-temperature thermal insulation and solid-oxide fuel cells.[3] On the other hand, this stability makes it difficult to achieve complete evaporation of zirconia in a thermal plasma, so up to now, not much work has been reported on the successful evaporation of solid ZrO_2.[4] The application of precursor powders with a mean particle size of 30 μm results in incomplete evaporation, which can be seen from transmission electron micrographs. In Fig. 1(a), unevaporated precursor particles (micron size) are surrounded by ultrafine material. Higher magnification of the ultrafine species shows particles of about 5 nm diameter (Fig. 1b).

Numerical modeling of the plasma zone and the behavior of the injected particles support the concept of the interaction between plasma properties (temperature and velocity field, gas flow, and gas composition), particle properties, as well as probe position and geometry.[5–10] Optical emission spectroscopy (OES) is an independent approach to check the numerically predicted particle evaporation experimentally.[10,11] The velocity of the injected particles and, thus, the residence time of the particles in the plasma plays an important role for evaporation. The velocity is measured by the laser Doppler anemometry (LDA) technique.

2. Experimental

The plasma reactor consists of a RF generator (frequency: 3.5 MHz, maximum RF plate power: 35 kW), a quartz plasma torch (50 mm outer quartz tube diameter), a quenching chamber, and a filter system. Details of the plasma processing are described elsewhere.[12] A schematic representation of the process is given in Fig. 2.

Spectroscopic measurements are performed with a setup similar to that used in Ref 10 for the spectroscopy of Ar/Cu plasmas. Yttria-stabilized zirconia (YSZ) is used as precursor powder, which is fed axially into the plasma by means of a water-cooled, stainless-steel powder injection probe. Two different injection modes are used; as listed subsequently.

Dry powder feeding (high feeding rate: approximately 60 g/h) is performed by means of a rotary wheel powder feeder. Agglomerated spray-dried YSZ powder (mean agglomerate size: 30 μm, supplier: Tosoh Corporation, Kaisoi-cho, Japan) with a carrier gas flow of 5 slm (standard liter per minute) is used in this mode.

The second method involves feeding of aqueous YSZ-powder suspensions (low feeding rate: $<$10 g/h YSZ) using an atomizer. Yttria-stabilized zirconia powders of 5 μm particle size (supplier: Unitec Ceramics Limited, Stafford, England) and deagglomerated spray-dried YSZ powder (primary particle size: $<$1 μm) with an atomizer gas flow of about 3 slm are used in these experiments.

P. Buchner, H. Schubert, J. Uhlenbusch, and **M. Weiss,** Institut für Laser und Plasmaphysik, Heinrich-Heine-Universität Düsseldorf, Universitätsstr. 1, D-40225 Düsseldorf, Germany. Contact e-mail: uhlenb@rz.uni-duesseldorf.de.

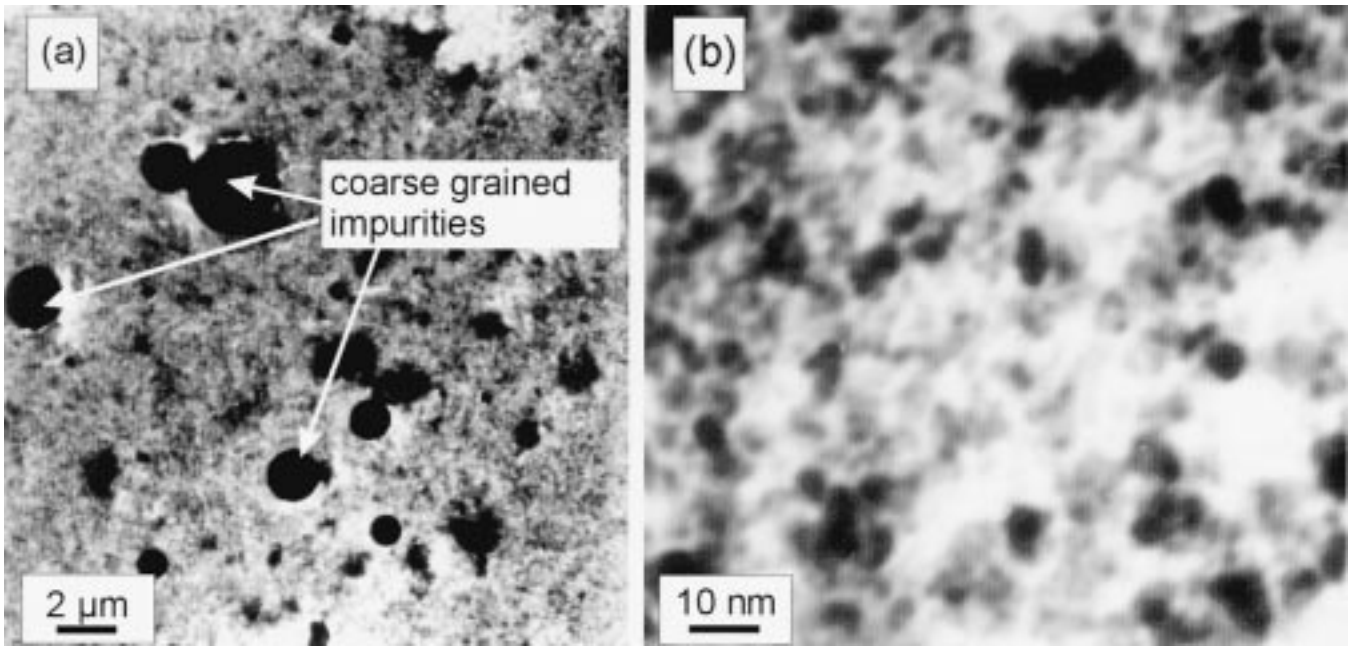

Fig. 1 Transmission electron micrograph of plasma prepared zirconia powders: (**a**) overview and (**b**) higher magnifications

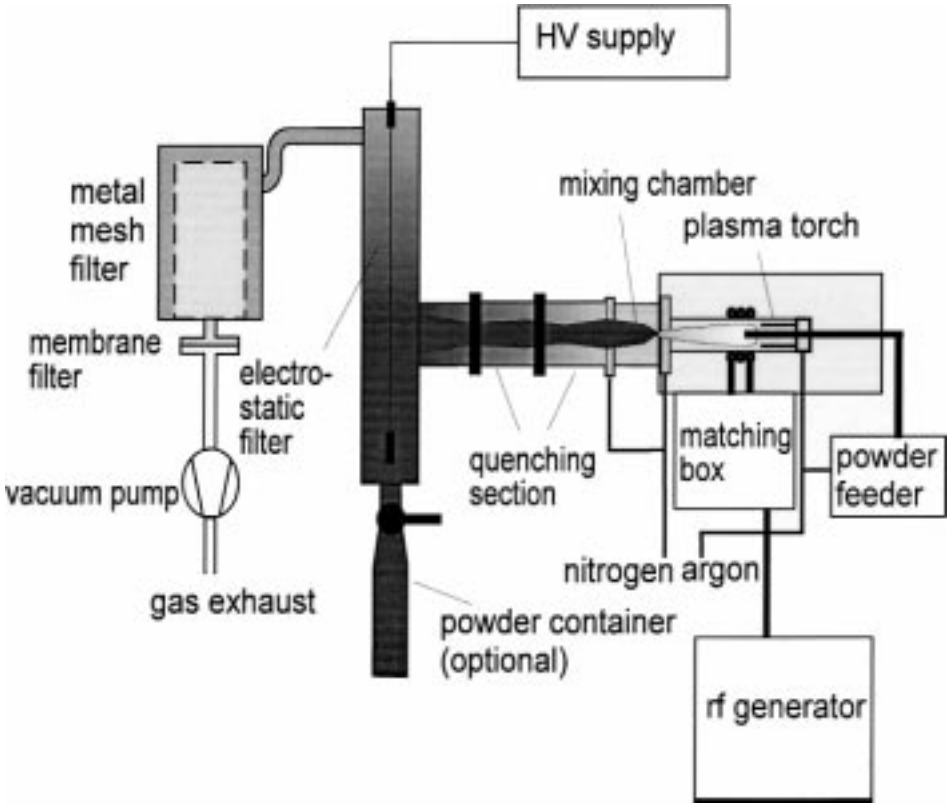

Fig. 2 Schematic representation of the thermal plasma process for the production of ultrafine powder

Yttrium lines were observed in the emission spectra, however, for the estimation of the particle evaporation, only the emission of zirconium was evaluated. Differences in evaporation of yttria and zirconia that might occur will be the subject of future studies. The light emitted side-on by the argon/zirconia plasma is imaged onto an optical fiber. The fiber entrance optics is mounted on a *y*-*z* stage, so that lateral (*y*) and axial (*z*) scans of the plasma can be performed. The fiber is coupled to a spec-

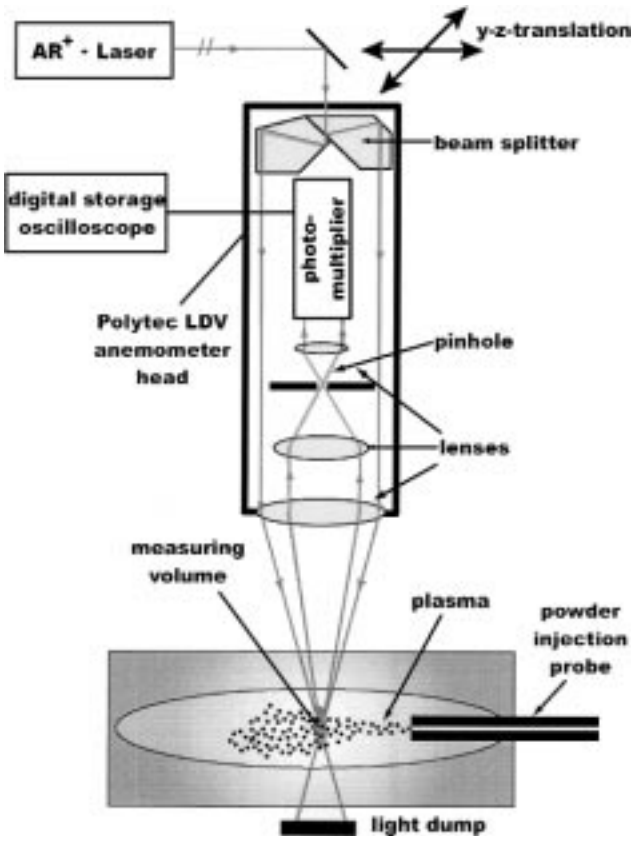

Fig. 3 Experimental setup for the LDA measurement

trograph, where an optical multi-channel analyzer (OMA) system detects the spectrally resolved signals. The emission signal is averaged over 10 to 20 scans to assure reproducible results. The time dependence of the plasma parameters, which also may influence the process, is not covered in this work.

The LDA is performed using an Ar ion laser (Model 166-1, Exciter Model 265, Spectra Physics GmbH, Darmstadt, Germany; maximum power approximately 1.5 W for the line at λ = 514.5 nm) and a commercial LDA head (laser Doppler velocimeter (LDV), Polytec, Waldbronn, Germany). Signal processing is done with a digital storage processor (LC 334a, LeCroy Corporation, Chestnut Ridge, NY). Doppler frequencies and, thus, particle velocities are deduced by a fast Fourier transform (FFT) of the measured scattered light intensity. The FFT is averaged over 100 samples. The experimental setup for the LDA measurements is described in Fig. 3.

3. Results and Discussion

3.1 Numerical Modeling

The model used for calculating the flow and temperature distribution of the plasma is similar to that given in Ref 7 and 13 and is described in detail elsewhere.[10] It is based on the simultaneous solution of equations of continuity, momentum (Navier-Stokes equation), and energy in combination with the Maxwell equations for the electromagnetic field.

The behavior of particles injected into the plasma is studied by calculation of particle trajectories and temperature history (heating-melting-evaporation), as described in Ref 10. Trajectories of particles corresponding to 50 different radial starting positions in the injection probe are used to calculate the spatial distribution of the flux of evaporated Zr atoms in the plasma (the ZrO_2 is assumed to dissociate immediately after evaporation). From this vapor flux density, $j_v(\mathbf{r})$, the density, n, of neutral Zr atoms in the plasma can be estimated and thus line-integrated spectral line emission can be calculated.

While an injected particle (diameter, d_p) travels through the plasma, the net heat transfer, Q, from the plasma onto the particle is determined by convective heating (heat transfer coefficient, h_c) and radiative losses:

$$Q = \pi d_p^2 h_c (T - T_p) - \pi d_p^2 \sigma_s \varepsilon (T_p^4 - T_a^4) \quad \text{(Eq 1)}$$

As described in Ref 7, T is the plasma temperature, T_p is the particle temperature, σ_s is the Stefan-Boltzmann constant, ε is the emissivity of the particle, and T_a is the ambient temperature.

To achieve a complete evaporation of an injected particle, the energy, W, transferred by the plasma onto the particle during the residence time, t_r, must be at least equal to the energy, E_v, required for heating, melting, and evaporating the particle.

There are four possibilities, as described subsequently, to increase the transferred energy in relation to E_v. The heat transfer coefficient, h (*e.g.*, addition of molecular gases), can be increased, and this results in a higher heat conductivity, k,[14] of the plasma. Since h is connected to k and the Nusselt number, Nu, and the particle diameter by

$$h = k \frac{\mathrm{Nu}}{d_p} \quad \text{(Eq 2)}$$

an improved heat transfer takes place.

The residence time, t_r, of the particles in the plasma can be increased by decreasing the particle velocity. This can be done by changing gas flow rates, process pressure, or the inner diameter of the injection probe.

The plasma temperature, $T(t)$, along the particle trajectory can be increased. Since higher temperatures in the entire plasma zone lead to unreasonably high RF power consumption (radiation losses show a sharp increase with temperature), only the plasma region near the particle trajectories should be heated. As will be shown below in this section, the decrease of carrier gas flow should cause an increase in temperature near the plasma axis according to model calculations.

The particle diameter of injected particles can be reduced. Since the heat transfer to the particle is proportional to the particle surface ($\sim d_p^2$), whereas the required heat to evaporate the particle is proportional to the particle volume ($\sim d_p^3$), smaller injected particles evaporate faster in the plasma than larger ones.

The residence time of the injected particles can be increased by decreasing the gas velocity in the central injection channel where the evaporating particles are concentrated. Calculations[15] show that the discharge pressure has nearly no effect on the axial temperature profile, while a reduction in carrier gas flow results in a temperature rise at smaller values of the axial coordinate. Thus, the high-temperature heating zone is extended in this case.

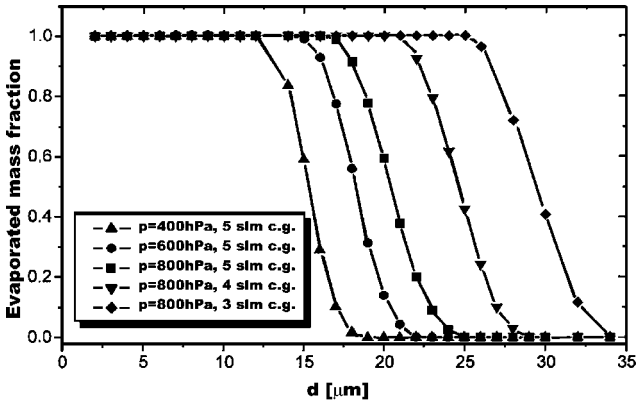

Fig. 4 Evaporated mass fraction at the end of the discharge region ($z = 200$ mm) vs initial particle diameter

As a consequence of the modified gas velocities and heating zone, the injected particles evaporate earlier in the plasma, when pressure is increased and carrier gas flow is reduced. The effect of changing pressure and carrier gas flow on the maximum particle size, which can be evaporated under these conditions, is shown in Fig. 4.

For particle sizes smaller than 10 μm, according to the calculations, complete evaporation takes place under all investigated conditions. By increasing the pressure, the maximum possible particle size is enhanced to approximately 15 μm. Reducing the carrier gas flow should allow the complete evaporation of particles up to 25 μm diameter. Disregarding the inner particle radial temperature profile, however, causes an overestimation of the evaporated mass fraction, which means that in reality only particles with a diameter below 10 μm evaporate.

Since precursor powders used for plasma processes normally show a broad particle distribution often specified by a maximum particle size (*e.g.*, determined by sieving), these rough data may suggest precursor powders suitable for processes where complete evaporation of the precursor is necessary.

3.2 Optical Emission Spectroscopy

Axial Intensity Measurements. Axial distributions of side-on line intensities of Zr emission at 535 nm are obtained for different powder-feed modes. Numerical calculations were performed for comparison. Three different particle-size distributions were used for modeling: (1) the broad distribution of the agglomerated spray-dried Tosoh powder ($d = 30$ μm), (2) the Unitec powder ($d > 5$ μm), and (3) a monodisperse powder of 1 μm size. The particle size distributions of the commercial powders were determined by light microscopy. The results for the axial line intensities are presented in Fig. 5(a) and (b). The axial coordinate, z, counts downstream from the end of the inner quartz tube of the plasma torch ($z = 0$).

Both measured and simulated data show the following two types of intensity distributions: large particles do not evaporate completely, thus, the corresponding intensity curve (circles in Fig. 5a and b) shows an increase in line intensity reflecting the rising amount of evaporated material. In contrast to this result, simulated and measured curves reveal a maximum of intensity for smaller, initial particle sizes. This curve type is caused by

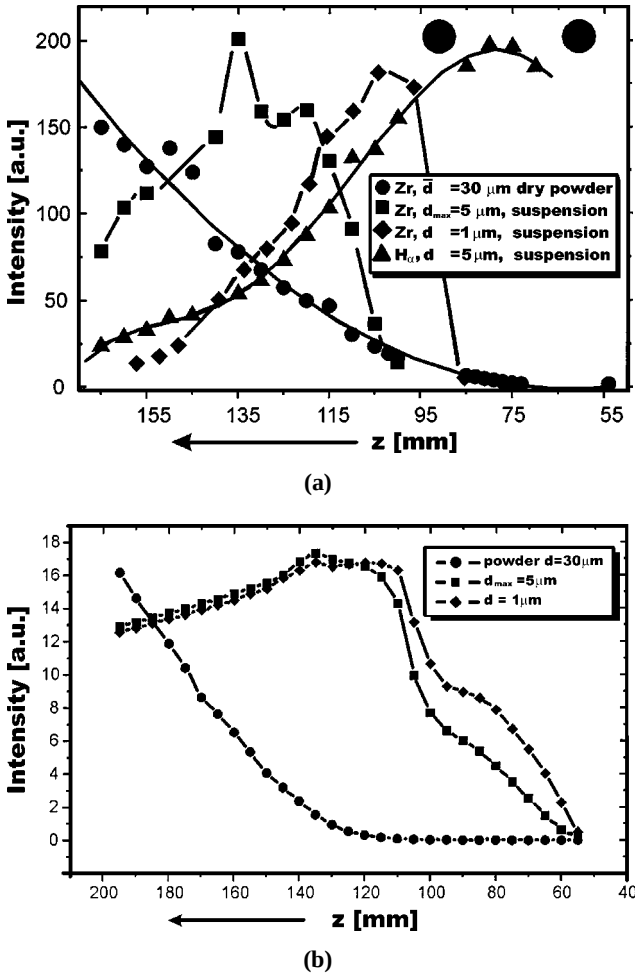

Fig. 5 (**a**) Side-on Zr line intensity for different feeding conditions: measurements, position of the injection probe: $z = 52$ mm; and (**b**) side-on Zr line intensity for different feeding conditions: simulation

complete evaporation of the small diameter particles; the temperature rise in the upstream part of the plasma creates an increase in line intensity in this plasma region. At the downstream end, plasma temperature drops connected with a decrease of Zr line emission. Measured and calculated profiles show a reasonable agreement. Discrepancies are only seen at large z values, where the intensity drop for smaller particles is less pronounced for the spectroscopic results compared with the modeling data. This might be attributed to the fact that the model neglects, besides the inner particle temperature profile, cooling effects by evaporation and dissociation of ZrO_2. This cooling leads to lower temperatures in the tail flame region, which decreases the emission intensity. If larger particles are present among the smaller ones, they pass the discharge only suffering partial evaporation.

The use of smaller particles for injection create an intensity rise at lower z positions in the plasma, which can be seen both from measured and simulated line intensities. The less pronounced drop in simulated line intensities at the downstream end of the plasma (compared to the measured values) might be attributed to the different conditions with respect to plasma composition in modeling and experiment. Thus, the introduction of water into the plasma changes the plasma properties (though the

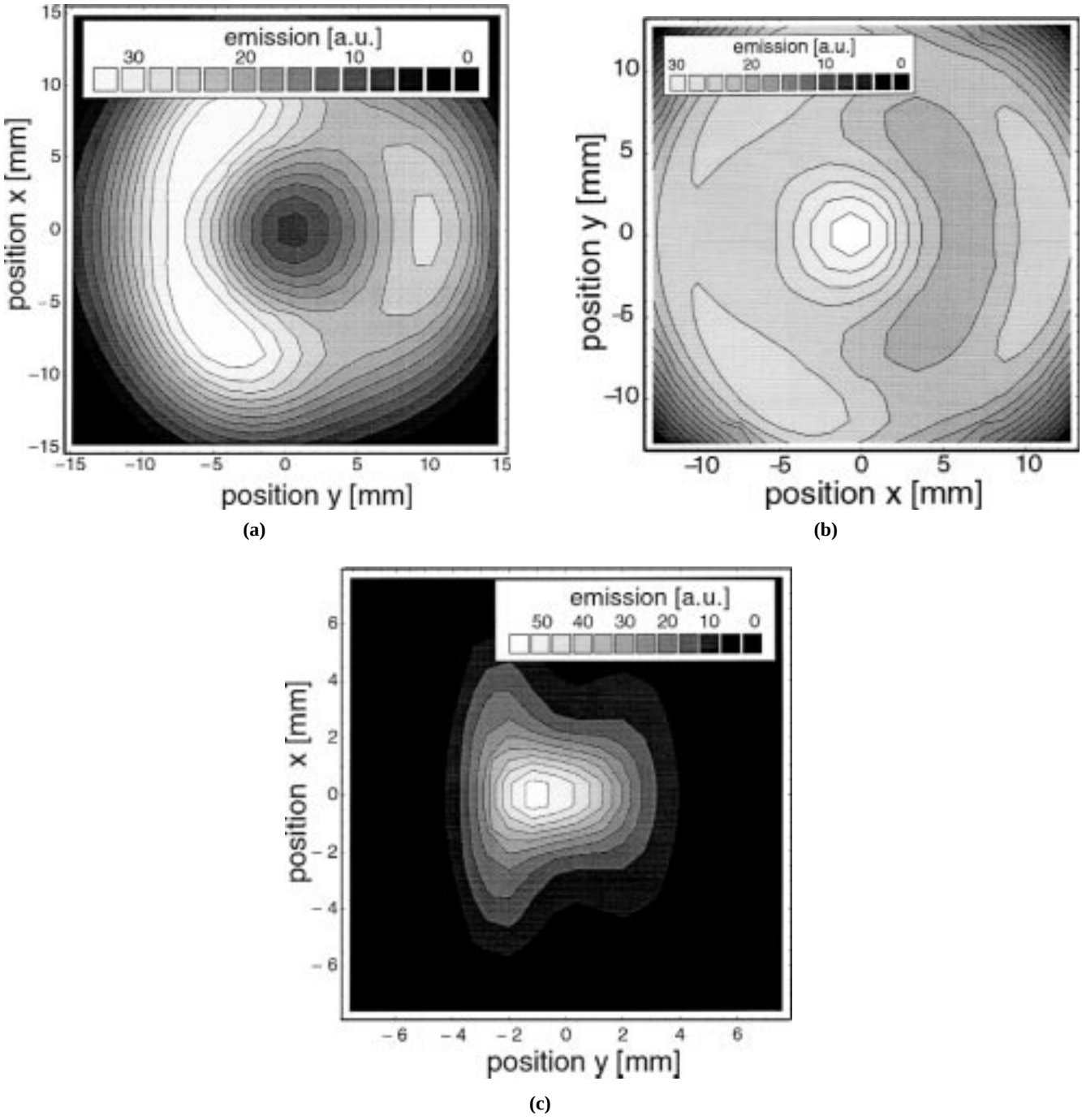

Fig. 6 (**a**) $\varepsilon(x, y)$, $z = 110$ mm, Ar emission (696.5 nm) during ZrO_2 powder feeding, (*b*) $\varepsilon(x, y)$, $z = 110$ mm, H_β emission (486.1 nm) during ZrO_2 suspension feeding, and (**c**) $\varepsilon(x, y)$, $z = 110$ mm, Zr emission (535.0 nm)

feed rates were extremely small, leading to a hydrogen content of the plasma of much less than 1%); therefore, the model calculations, which assume a pure argon plasma, show deviations from the measurements.

Radial Emission Distribution. The emission coefficients of the spectral lines were calculated by asymmetrical Abel inversion[16] of measured side-on line intensities. Asymmetries in the plasma emission may be caused, for example, by asymmetric power coupling, which is unavoidable in common induction coil geometries, by misalignment of the powder injection probe or by asymmetries in the gas flow.

The steps of the evaluation are as follows. The measured lateral data are approximated by a set of trigonometric functions, centered and background subtracted. Then, the symmetric part, I_s, was extracted and inverted conventionally. The asymmetry function is multiplied by the result to get asymmetrical distribu-

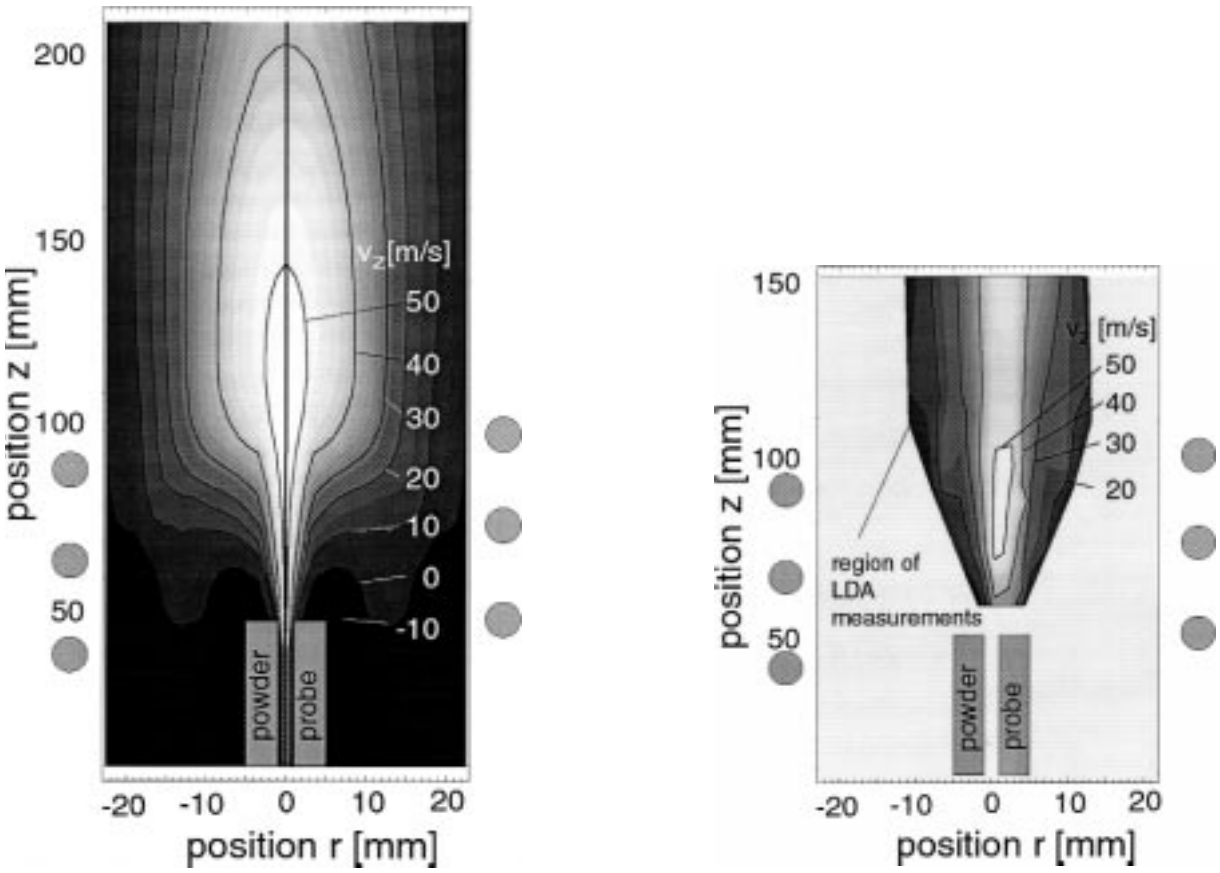

Fig. 7 (**a**) Distribution of the axial velocity component obtained by modeling and (**b**) distribution of the axial velocity component obtained by LDA measurements

tions of the emission coefficient. Details of the procedure are described elsewhere.[15] In these calculations, only asymmetries perpendicular to the line of sight (*y* direction) are considered. Asymmetries in the direction of the line of sight (*x* direction) are suppressed, *i.e.*, symmetry in the *x* direction is forced by the method of measurement and evaluation. This is somehow arbitrary, since, under real plasma conditions, asymmetry appears not necessarily only in the *y* direction but may also occur in the direction of the line of sight. However, compared to the conventional symmetric Abel inversion, this method shows more details of the emission distribution with a minimum of additional numerical effort. A better look at the distribution could be given by tomographic methods,[17,18] which are much more costly both experimentally and numerically.

Asymmetric emission distributions of Ar, H, and Zr have been measured at a fixed axial position ($z = 110$ mm, *i.e.*, approximately 2 cm downstream the induction coil region). The results are presented in Fig. 6.

All the figures show asymmetries in the profiles. Significant differences in the distribution of the three species can be seen. Ar emission shows a hollow profile corresponding to a cold central-injection channel that lowers emission near the plasma center.

The profiles of the injected species H and Zr show on-axis maxima due to the location of injection. While H emission nearly fills the entire Ar plama region, Zr emission concentrates on the plasma center (notice the different scales in Fig. 6a to c). This indicates the delayed production of Zr from ZrO_2 compared to a nearly immediate dissociation of the injected water. The radial diffusion acts on the dissociated material much faster than on solid or liquid particles.

3.3 Laser Doppler Anemometry

The Doppler signal is measured at 110 *y*-*z* positions in the plasma region. The values of the axial velocity component are interpolated to obtain a two-dimensional distribution. The lines of constant axial velocities are compared with model calculations in Fig. 7.

The region of LDA measurements is restricted to the area where injected particles are present. Both LDA and modeling reveal a central injection channel that has higher velocities than the surrounding plasma region. This channel is important for the prevention of particle movement around the hot plasma zone. On the other hand, the high velocities decrease the residence time in the plasma. A more detailed presentation of the velocity in the central channel is given in Fig. 8.

The results of the LDA measurements are nearly consistent with the modeling results. Since particles with $d_0 > 30$ μm are present in the precursor powder, LDA measurements can be per-

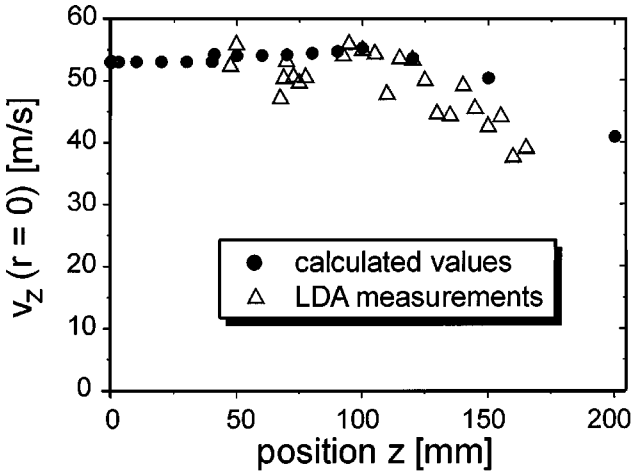

Fig. 8 Centerline axial velocity: LDA measurements and modeling results

formed at all visible axial plasma positions, *i.e.*, unevaporated particles are present in the product in this mode. For the broad particle-size distribution of the precursor powder, differences in particle velocities plasma may occur, since the larger particles cannot follow the plasma flow exactly. This effect was studied by modeling, results are given in Fig. 9. The differences in velocity for particles injected on-axis are up to several m/s, especially in the tail region of the plasma where plasma velocities strongly decrease, and heavier particles do not decelerate by the same factor. For particles up to 15 μm, only small differences between plasma and particle velocities are found. Further measurements are planned to investigate the influence of plasma and particle parameters on the velocity distribution and, thus, the residence time, especially when using more complex plasma compositions, such as suspension-loaded plasmas, where modeling is more difficult.

4. Summary and Conclusions

The heating and evaporation of zirconia injected into a thermal RF plasma reactor is studied by numerical modeling, OES, and LDA. Two different injection modes are used: dry powder feeding and suspension feeding.

Modeling results indicate that particle size of the injected species and plasma conditions (especially carrier gas flow) can be chosen properly to achieve complete precursor evaporation. Spectroscopic measurements confirm this for a small particle suspension, though up to now with a low feeding rate.

Axial emission profiles obtained experimentally and numerically are in qualitative agreement, showing a continuously growing intensity if large particles are involved, and intensity profiles with pronounced maxima, if precursor powder contains smaller particles.

Two-dimensional profiles of the Ar, H, and Zr emission at one common axial position show that Zr is concentrated near the axis, while H fills nearly the entire plasma region. The Ar hollow profile indicates a cold injection channel, which is also determined by numerical modeling and the LDA measurements. This channel determines the residence time of the injected precursor. Thus, further work will be carried out on the analysis of

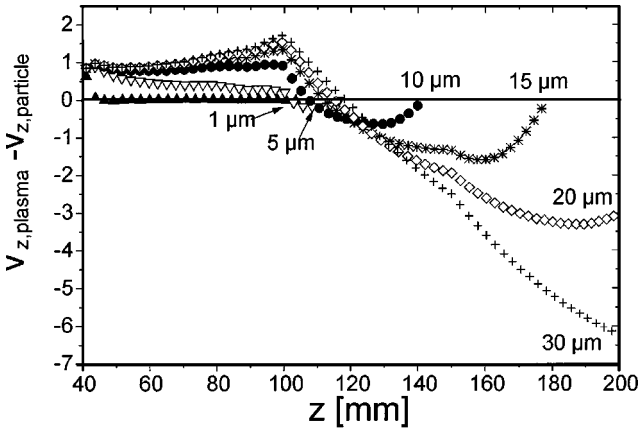

Fig. 9 Difference between axial velocities of particles and plasma for different initial particle diameters

the interaction between process parameters and the character of the injection channel, measured by LDA and emission spectroscopy.

Acknowledgments

Thanks to the Forschungszentrum Jülich (Drs. R. Vassen and H.J. Penkalla) for performing transmission electron microscopy. This work is supported by the Bundesministerium für Bildung und Forschung under Contract No. 13N7408/3.

References

1. T. Yoshida: *Mater. Trans. A*, 1990, vol. 21A, pp. 1-11.
2. I. Barin and O. Knacke: *Thermochemical Properties of Inorganic Substances*, Springer, Berlin, 1973.
3. J.S. Lee, T. Matsubara, T. Sei, and T. Tsuchiya: *J. Mater. Sci.*, 1997, vol. 32, p. 5249.
4. J. Grabis, A. Kuzjukevics, D. Rasmane, M. Mogensen, and S. Linderoth: *J. Mater. Sci.*, 1998, vol. 33, p. 723.
5. M.I. Boulos: *IEEE Trans. Plasma Sci.* PS-4, 1976, vol. 28.
6. T. Yoshida and K. Akashi: *J. Appl. Phys.*, 1977, vol. 48, p. 2252.
7. P. Proulx, J. Mostaghimi, and M.I. Boulos: *J. Heat Mass Transfer*, 1985, vol. 28, p. 1327.
8. P. Proulx, J. Mostaghimi, and M.I. Boulos: *Coll. Phys.*, C5, 1990, pp. 263-70.
9. S. Girshick and W. Yu: *Plasma Chem. Plasma Processing*, 1990, vol. 10, p. 515.
10. P. Buchner, H. Ferfers, H. Schubert, and J. Uhlenbusch: *Plasma Sources Sci. Technol.*, 1997, vol. 6, p. 450.
11. D.V. Gravelle, M. Beaulieu, M.I. Boulos, and A. Gleizes: *J. Phys. D, Appl. Phys.*, 1989, vol. 22, pp. 1471-77.
12. P. Buchner, D. Lützenkirchen-Hecht, H.-H. Strehblow, and J. Uhlenbusch: *J. Mater. Sci.*, 1999, vol. 34, pp. 925-31.
13. J. Mostaghimi, P. Proulx, and M.I. Boulos: *Plasma Chem. Plasma Processing*, 1984, vol. 4, p. 199.
14. M.I. Boulos, P. Fauchais, and E. Pfender: *Thermal Plasmas—Fundamentals and Applications*, Plenum Press, New York, NY, 1994.
15. P. Buchner, H. Schubert, J. Uhlenbusch, and K. Willée: *Plasma Chem. Plasma Processing*, 1999, vol. 19, pp. 341-62.
16. M.W. Blades: *Appl. Spectr.*, 1983, vol. 37, p. 371.
17. N.R. Sauthoff and S. von Goeler: *IEEE Trans. Plasma Sci.*, PS-7, 1979, vol. 3, pp. 141-47.
18. T. Neger: *J. Phys. D: Appl. Phys.*, 1995, vol. 28, pp. 47-54.